

Broadband spectral and temporal study of Ton 599 during the brightest January 2023 flare

Aaqib Manzoor^{1*}, Zahir Shah^{2†}, Sunder Sahayanathan^{3,4}, Naseer Iqbal¹ & Athar A. Dar^{1,2}

¹Department of Physics, University of Kashmir, Srinagar 190006, India.

²Department of Physics, Central University of Kashmir, Ganderbal 191201, India.

³Astrophysical Sciences Division, Bhabha Atomic Research Center, Mumbai 400085, India.

⁴Homi Bhabha National Institute, Mumbai 400094, India.

Accepted XXX. Received YYY; in original form ZZZ

ABSTRACT

In this work, we provide a detailed analysis of the broadband temporal and spectral properties of the blazar Ton 599 by using the observations from *Fermi*-LAT and *Swift*-XRT/UVOT telescopes, during its brightest γ -ray flaring. The one-day bin γ -ray light curve exhibits multiple substructures with asymmetric and symmetric profiles. Notably, the γ -ray light curve shows a maximum flux of $3.63 \times 10^{-6} \text{ ph cm}^{-2} \text{ s}^{-1}$ on MJD 59954.50, which is the highest flux ever observed from this source. The correlation between the γ -ray flux and γ -ray spectral indices suggests a moderate harder when the brighter trend. Taking γ -ray light curve as the reference, a strong correlation is observed with X-ray, optical, and UV energies. Additionally, the γ -rays and optical/UV emissions exhibit higher variability compared to X-rays. To understand the parameter variation during the active state of the source, we conducted a statistical broadband spectral modelling of the source in 10 flux intervals of equal duration. A one-zone leptonic model involving synchrotron, synchrotron-self-Compton, and external-Compton processes successfully reproduces the broadband SED in each of these flux intervals. We observed that the flux variation during the active state is mainly associated with the variation in the magnetic field and the particle spectral indices.

Key words: radiation mechanisms: non-thermal – galaxies: active – individual: Ton 599 – gamma-rays: galaxies.

1 INTRODUCTION

Blazars are radio-loud Active Galactic Nuclei (AGN) with a powerful relativistic jet inclined close to the observer’s line of sight. These are powered by a supermassive black hole (SMBH) located at their centre (Urry & Padovani 1995). The small angle of inclination of the relativistic jet induces Doppler boosting in blazar emission, leading to distinctive observational features in all the energy bands (Böttcher et al. 2013; Ulrich et al. 1997). The temporal variability of blazars extends from years (Raiteri et al. 2013) to minutes (Aharonian et al. 2007; Albert et al. 2007). Blazars are categorized into two main classes: Flat Spectrum Radio Quasars (FSRQs) and BL Lacertae (BL Lacs) objects, FSRQs are characterised by prominent emission line features, whereas BL Lacs typically display either weak or no emission line features (Urry & Padovani 1995).

Blazars display a distinctive broadband spectral energy distribution (SED) marked by two prominent broad peaks. The first peak is typically observed in the Optical/UV/X-ray energy spectrum, while the subsequent peak is observed in the γ -ray energy range (Fossati et al. 1998; Mao et al. 2016). The lower energy peak results from the synchrotron cooling of electrons within the blazar jet, while investigations into the precise mechanisms governing the high energy emission are still ongoing. The high energy peak in the SED is generally associated with the inverse-Compton (IC) scattering

(Abdo et al. 2010b). The seed photons for IC scattering can be the synchrotron photons from the jet, and IC scattering of synchrotron photons is described as synchrotron-self-Compton process (SSC: Jones et al. 1974; Ghisellini et al. 1985; Costamante & Ghisellini 2002)). They can also originate from outside the jet, and IC scattering of these photons is described as an external-Compton process (EC: Dermer et al. 1992; Sikora et al. 1994; Błażejowski et al. 2000; Shah et al. 2017a)). The outside photon sources primarily include the broad line region (BLR: Ghisellini & Madau 1996), dusty torus (Błażejowski et al. 2000; Ghisellini & Tavecchio 2008) and accretion disk (Dermer & Schlickeiser 1993; Boettcher et al. 1997). In some cases, the high energy component of blazar SED is explained with a hadronic model through proton synchrotron process and/or by pion decay processes (Mannheim & Biermann 1992; Mannheim 1993; Mücke & Protheroe 2001; Mücke et al. 2003). Generally, the preference for the leptonic model over the hadronic model typically stems from the considerable jet power demanded by the latter. (Böttcher et al. 2013; Petropoulou & Dermer 2016). The peak synchrotron frequency (ν_{syn}^p) for blazars in the $\nu - \nu f_\nu$ plot is an important observational feature that distinguishes FSRQs from BL Lacs (Fossati et al. 1998). For FSRQs ν_{syn}^p ranges between $10^{12.5}$ and $10^{14.5}$ Hz, while in BL Lacs its value is between 10^{13} and 10^{17} Hz (Abdo et al. 2010b). BL Lacs are categorised into three groups depending on the position of ν_{syn}^p within the SED: low-energy peaked BL Lacs (LBL) if ν_{syn}^p is below 10^{14} Hz, intermediate-energy peaked BL Lacs (IBL) if ν_{syn}^p falls between 10^{14} Hz and 10^{15} Hz, and high-

* E-mail: aqibmanzoor1111@gmail.com

† E-mail: shahzahir4@gmail.com

energy peaked BL Lacs (HBL) if ν_{syn}^p exceeds 10^{15} Hz (Abdo et al. 2010b).

Ton 599, identified as a bright FSRQ, is situated at a redshift $z \sim 0.725$ (Hewett & Wild 2010). Positioned at equatorial coordinates R.A = 179.883 and Dec. = 29.2455 degrees, it was first detected by the Energetic Gamma Ray Experiment Telescope (EGRET) in γ -ray energy (Thompson et al. 1995). Following the launch of the *Fermi*-LAT satellite, Ton 599 was detected within the first three months (Abdo et al. 2010a). Remarkably, it stands out as one of the few FSRQs detected in TeV energies (Mukherjee & VERITAS Collaboration 2017; Mirzoyan 2017). This source has been also observed in other energy bands over the past three decades, with a primary focus on investigating the flux variability. The SSC model was employed in the early 1980s to explain the radio and γ -ray emission from the source (Glassgold et al. 1983). The study carried out by McHardy et al. (1993) on Ton 599 suggests that the relativistic jet which initially is inclined at a very small angle with respect to the observer undergoes a small bending at later stages. Ramakrishnan et al. (2014) carried out a correlation analysis between the radio and γ -ray energy bands with the aim of constraining the size of the γ -ray emitting region. Several studies, such as Celotti & Ghisellini (2008); Ghisellini et al. (2014); Paliya et al. (2017) have employed a one-zone model to perform broadband SED modelling of the source. The primary objective of these studies was to explore the power of jets and other parameters of blazars in different flux intervals. In November 2017, the Ton 599 underwent a prolonged flare for the first time across the electromagnetic spectrum. During this flare, the γ -ray flux reached the maximum of $1.26 \times 10^{-6} \text{ ph cm}^{-2} \text{ s}^{-1}$ (Prince 2019). A detailed multi-frequency variability study of this flare was carried out by Prince (2019), while the same flare was modelled using the leptonic model by Patel & Chitnis (2020). They constrained the origin of γ -rays to be outside the BLR region and estimated the size of the emission region as $\sim 1.03 \times 10^{16}$ cm. Recently, the Ton 599 displayed its brightest ever γ -ray flare in January 2023. This flare was simultaneously observed in optical/UV and X-ray energy bands by *Swift*-UVOT and *Swift*-XRT, thereby allowing us to carry out a detailed multi-wavelength temporal and spectral study of this flaring period.

In this work, we carry out a detailed multi-wavelength temporal and spectral study of Ton 599 for the January 2023 flare. This paper consists of 5 Sections. In section 2, we give details of the data analysis procedure and observations used in this work. In section 3, we present the temporal properties of the source. In section 4, we provide the spectral properties of the source. Finally, the summary and discussion of results are given in section 5.

2 OBSERVATIONS AND DATA ANALYSIS

To investigate the temporal and spectral characteristics of the January 2023 flare in Ton 599, we utilized data from *Swift*-Ultraviolet/Optical Telescope (UVOT; Roming et al. 2005), X-ray telescope (XRT; Burrows et al. 2005) and *Fermi*-LAT (Atwood et al. 2009) telescope. The following section provides details of the data analysis techniques and instruments utilized in this study.

2.1 *Fermi*-LAT Analysis

The *Fermi*-LAT is an integral component of the *Fermi* γ -ray space telescope, a satellite launched by NASA in 2008. Operating within the energy range of 20 MeV to 300 GeV, it is designed to detect and study γ -rays. It converts the γ -ray photons into electron-

positron pairs. It possesses a broad field of view of around ~ 2.3 Sr. To study the January 2023 flare, we conducted an analysis using the *Fermi*-LAT PASS 8 data obtained during the period MJD 59884–59992. This data is publicly available at HEASARC ¹. We selected a circular area with a radius of 15 deg around the location of Ton 599 as the region of interest (ROI). Photons gathered within the energy span of 0.1 – 300 GeV are taken into consideration. The *fermipy*-v1.0.1 (Wood et al. 2017) and the instrument function (IRF) *P8R3_SOURCE_V3* are used for analyzing the data. For analysis, we adhered to the standard procedure outlined in *Fermi*-LAT documentation ². To take care of the earth limb contamination, the zenith angle was chosen to have a maximum value of 90 degrees. We acquired a model file that contains all the sources given in the *Fermi*-LAT 4FGL catalogue. During analysis, the model parameters of all sources which fall within ROI were kept free, whereas, for sources lying beyond ROI, the model parameters were frozen to their 4FGL catalogue values. To account for galactic and isotropic emission contributions, *gll_iem_v07.fits* and *iso_P8R3_SOURCE_V3_v1.txt* were added to the model file during fitting. The good time intervals (GTI) were selected using a recommended criteria of “(DATA_QUAL > 0)&&(LAT_CONFIG == 1)”. For γ -ray spectral and light curve generation, source detection is considered only when test statistics (TS) is > 9 ($\sim 3\sigma$ detection; Mattox et al. 1996). In this work, we have obtained a one-day binned γ -ray light curve of Ton 599 during the period MJD 59884–59992. Additionally, we acquire the γ -ray spectra of the source during the simultaneous X-ray and optical/UV observations for the broadband spectral analysis.

2.2 *Swift*-XRT/UVOT

The *Swift* is a multi-wavelength satellite launched by NASA on the 20th of, November 2004 to monitor transient events occurring in both the galactic and extra-galactic skies. It possesses a viewing angle of 23.6×23.6 arcmins. Featuring an effective area of 110 cm² and a resolution of 18 arcseconds, the satellite consist of three onboard telescopes (Roming et al. 2005; Burrows et al. 2005). The *Swift* observed the January 2023 flare of Ton 599 in Ultraviolet/Optical and X-ray energy bands. The data is publicly available at HEASARC ³. The details of the observations carried out during the January 2023 flaring period of Ton 599 are given in Table 1.

In the case of *Swift*-XRT, the clean event files were generated by running *xrtpipeline*, utilizing the calibration file (CALDB, version: 20190910). The *xselect* package is employed for selecting the source and background regions, as well as for the subsequent generation of the spectra of these regions. The source region is defined as a circular area with a radius of 25 pixels, centred at the source position. Similarly, the background region is also circular, with a radius of 50 pixels, positioned in a region devoid of the source. An auxiliary response file (ARF) is generated using *xrtmkarf*. The spectra have been grouped using the *grppha* tool, ensuring that each bin contains a minimum of 20 counts. Subsequently, the grouped spectra within the energy range of 0.3-10 keV were fitted using *xspec* (Arnaud 1996), a component of the HEASoft package (version 6.30.1). The spectra were fitted by employing an absorbed power-law model. During the spectral fitting, the neutral hydrogen column density n_H is frozen at $1.63 \times 10^{20} \text{ cm}^{-2}$ (Kalberla et al. 2005), while other parameters are

¹ <https://fermi.gsfc.nasa.gov/cgi-bin/ssc/LAT/LATDataQuery.cgi>

² <http://fermi.gsfc.nasa.gov/ssc/data/analysis/>

³ <https://heasarc.gsfc.nasa.gov/cgi-bin/W3Browse/w3browse.pl>

set free.

The *Swift*-UVOT has also observed the January 2023 flare of Ton 599 utilizing the available six filters. The *uvotsource* package incorporated within HEASoft (version 6.30.1) was used to analyze the UVOT data. Multiple images within a filter were combined using the *uvotsum* tool. Photons originating from the source were collected from a circular region of 5 arcsec radius, centred at the source position. In contrast, background photons were obtained from a circular region with a 10 arcsec radius, located in a source-devoid region. The multiple images in a filter are added with *uvotsum* tool. The observed flux points are de-reddened for galactic extinction, by the procedure outlined by [Schlafly & Finkbeiner \(2011\)](#).

3 RESULTS

3.1 Temporal study

To investigate the temporal features of Ton 599, we generated its multi-wavelength light curves (MWL LC) in UV/optical, X-ray, and γ -ray energy bands during the period MJD 59884 – 59992. The daily binned γ -ray light curve is obtained by integrating photons within the 0.1 – 300 GeV. The Ton 599 has been observed across multiple wavelengths during the period MJD 59943 – 59974. Figure 1 displays the MWL LC of the Ton 599 by using the *Fermi* and *Swift* observations. The base-flux in γ -ray light curve is obtained as 2.9×10^{-7} ph cm $^{-2}$ s $^{-1}$, which is calculated by taking the average of fluxes in the quiescent state during the time interval MJD 59885 – 59904. We define the active state of the source as the period where the γ -ray flux has enhanced significantly above the base flux and multi-wavelength observations are available. As shown in Figure 2, γ -ray flux during the time interval MJD 59943-59974 has increased significantly above the base-flux. We call this time interval an active state of the source. In the daily binned γ -ray light curve, the source has shown a peak flux of 3.63×10^{-6} ph cm $^{-2}$ s $^{-1}$ on MJD 59954.50. This is the highest-ever flux reported from Ton 599 till now. It is about ~ 13 times larger than the base flux of the source. A closer look at a one-day binned γ -ray light curve (see Figure 2) shows that a light curve consists of five dominant component shape, we name them C1, C2, C3, C4, and C5. We fit these components by an exponential function of the form ([Abdo et al. 2010c](#))

$$F(t) = F_b + \frac{2F_0}{\left[\exp\left(\frac{t_0-t}{T_r}\right) + \exp\left(\frac{t-t_0}{T_d}\right) \right]}, \quad (1)$$

to calculate the rise and decay time of these components. Here F_b represents base flux, t_0 is the peak time, F_0 is peak flux, T_r and T_d represent the rise and decay times of the individual components, respectively. The fitted profile of the light curve is shown in Figure 2, and the best-fit parameters are shown in Table 2. Additionally, we have calculated the asymmetric parameter (ζ) for each component. The asymmetric parameter measures the strength of symmetry in each component. It varies between 0 – 1 and is given by $\zeta = \frac{T_d - T_r}{T_d + T_r}$. A component is said to be symmetric if $\zeta < 0.3$, moderately symmetric if $0.3 < \zeta < 0.7$ and asymmetric if $\zeta > 0.7$. The calculated values of ζ parameter are given in Table 2, the results suggest that the components C1, C2, and C3 are symmetric, while the component C4 is asymmetric. However, due to substantial error in the asymmetric parameter value of component C5, its profile is categorized as both symmetric and moderately asymmetric.

Following the detection of high γ -ray activity by *Fermi*-LAT, *Swift* conducted 10 observations of the Ton 599 source during its

active state (MJD 59943-59974), the description of these observations is given in Table 1. We use these observations to investigate the behaviour of the source at optical, UV, and X-ray energy bands. The X-ray, optical, and UV light curves are presented in the second, third, and fourth panels of the MWL LC respectively (Figure 1). The X-ray data points are acquired within the energy range of 0.3 – 10 keV, with each point in these light curves representing a specific observation ID. The visual inspection of MWL LC (see Figure 1) suggests correlated flux variations within different energy bands. We look for the correlation between γ -ray flux and other energy bands by taking the γ -ray flux as a reference and utilizing the Spearman rank correlation method. The resulting r_s and P_{rs} listed in Table 3 confirm the presence of correlated flux variations across distinct energy bands.

Blazars show variability in all the observed energy bands. These variations are prominent during flaring events. The variability amplitude depends upon source parameters *viz* magnetic field, viewing angle, and particle density ([Kaur & Baliyan 2018](#)). The availability of multi-wavelength observations in optical, ultraviolet, X-ray, and γ -rays for Ton 599 facilitates a comparison of variability amplitudes across different energy bands. The fractional variability was calculated by following ([Vaughan et al. 2003](#))

$$F_{var} = \sqrt{\frac{S^2 - \langle \sigma_{err}^2 \rangle}{\langle F \rangle^2}}, \quad (2)$$

where S^2 , $\langle F \rangle$, and $\langle \sigma_{err}^2 \rangle$ are flux variance, mean flux and mean square error in the measurement of flux respectively. The uncertainty in the F_{var} is estimated using the formalism described in [Poutanen et al. \(2008\)](#)

$$\Delta F_{var} = \sqrt{F_{var}^2 + err(\sigma_{NXS}^2)} - F_{var}, \quad (3)$$

where

$$err(\sigma_{NXS}^2) = \sqrt{\left(\sqrt{\frac{2}{N}} \cdot \frac{\langle \sigma_{err}^2 \rangle}{\langle F \rangle^2} \right)^2 + \left(\sqrt{\frac{\langle \sigma_{err}^2 \rangle}{N}} \cdot \frac{2F_{var}}{\langle F \rangle} \right)^2}, \quad (4)$$

where N is the total number of flux points in the light curve. The calculated values of F_{var} and their corresponding uncertainties ΔF_{var} for optical, ultraviolet, X-ray, and γ -ray bands are given in Table 4. As shown in the plot between F_{var} and energy (see Figure 3), the F_{var} shows a dip at X-rays and then increases again towards the GeV band. This dip at X-rays has been also reported by many authors in other blazar sources ([Chidiac et al. 2016](#); [Baloković et al. 2016](#); [Shah et al. 2021a,a](#); [Malik et al. 2022a](#)). The X-ray dip is linked to FSRQs' SED shape: high-energy electrons dominate optical/UV and γ – ray emissions via synchrotron and IC losses, respectively, while X-rays result from IC losses due to the low-energy electrons. Since the highly energetic electrons cool faster, this results in a larger F_{var} at optical/UV and GeV bands than at the X-ray band.

3.2 The gamma-ray spectral behaviour

The one-day binned γ -ray light curve (see Figure 2) has been obtained by fitting the spectrum (0.1 – 300 GeV) with a log-parabola model defined as

$$\frac{dN}{dE} = N_0 \left(\frac{E}{E_p} \right)^{-\alpha - \beta \log\left(\frac{E}{E_p}\right)}, \quad (5)$$

where α is the index at the pivot energy E_p , and β is the curvature parameter. The index values obtained by fitting the daily averaged

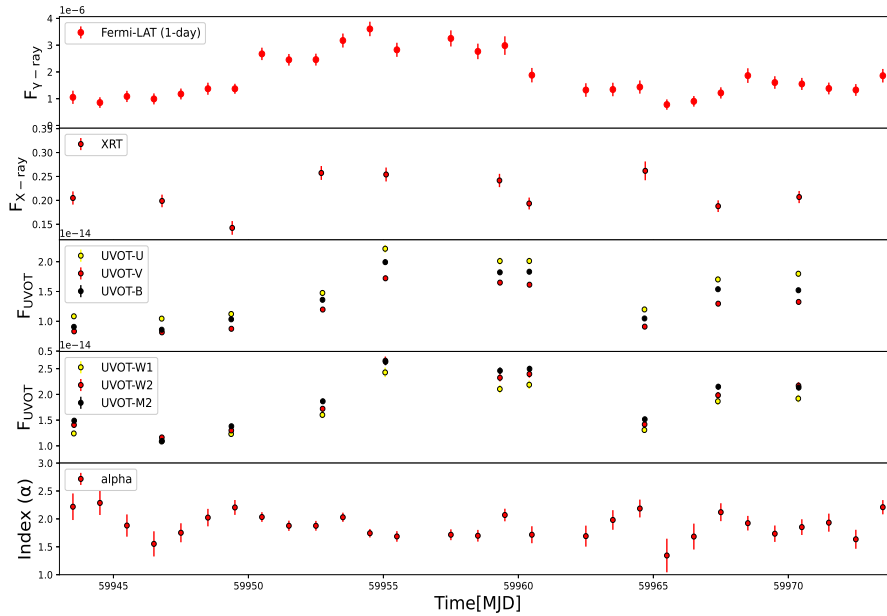


Figure 1. Multi-wavelength light curves for Ton 599 during MJD 59943-59974, featuring (1) top panel: daily-binned γ -ray light curve (0.1–300 GeV) from Fermi-LAT (with unit $\text{ph cm}^{-2} \text{s}^{-1}$), (2) second panel: X-ray light curve (0.3–10.0 keV) from *Swift*-XRT (counts/sec), (3) third and fourth panel: Optical/Ultraviolet light curves from *Swift*-UVOT in $\text{erg cm}^{-2} \text{s}^{-1} \text{\AA}^{-1}$. The final panel presents the temporal evolution of spectral slope values.

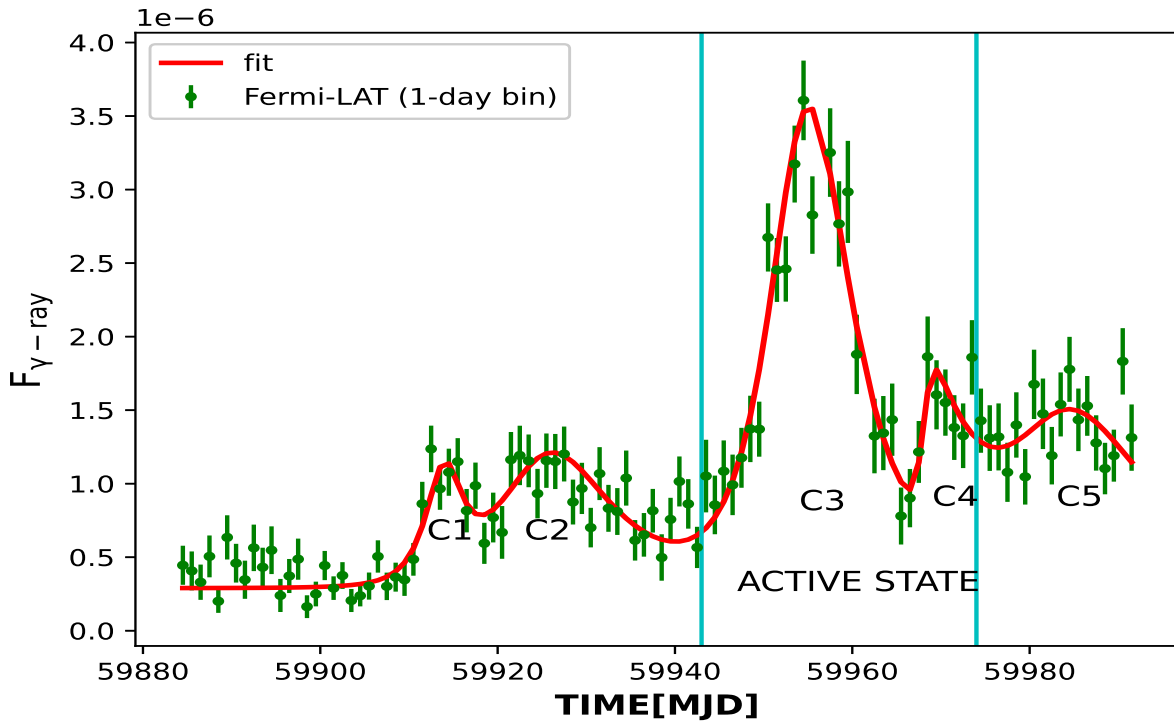


Figure 2. The daily-binned γ -ray light curve of Ton 599 obtained in the energy range of 0.1 – 300 GeV during the period MJD 59884 – 59992. The γ -ray flux is in units of $\text{ph cm}^{-2} \text{s}^{-1}$. The solid red curve shows the best fit, which is the sum of exponential functions. The period delineated by two vertical cyan-coloured lines, corresponding to MJD 59943 – 59974, represents the active state of the source.

Table 1. Details of *Swift*-XRT/UVOT observations.

S. No.	Observation ID	Time (MJD)	XRT exposure (ks)	UVOT exposure (ks)
1.	00036381097	59943.5	1.41	1.38
2.	00036381098	59946.8	1.49	1.47
3.	00036381099	59949.4	1.01	0.98
4.	00036381100	59952.7	1.58	1.55
5.	00036381101	59955.1	1.59	1.52
6.	00036381102	59959.3	1.78	1.70
7.	00036381103	59960.4	3.82	3.75
8.	00036381104	59964.7	1.53	1.50
9.	00036381105	59967.4	1.62	1.60
10.	00036381106	59970.4	1.67	1.65

Table 2. Rise and decay times of different components of γ -ray light curve for Ton 599 during the time MJD 59884–59992. Column: 1. Component, 2. Peak time (MJD), 3. Peak flux, 4. Rise time 5. Decay time and 6. Asymmetry parameter.

Components	t_0 (MJD)	F_0 (10^{-6} ph cm $^{-2}$ s $^{-1}$)	T_r (days)	T_d (days)	$ \zeta $
C1	59914	0.7	1.78 ± 0.43	1.69 ± 0.62	0.025 ± 0.28
C2	59925	0.9	4.61 ± 0.90	7.04 ± 0.62	0.20 ± 0.09
C3	59954.44	3.2	3.49 ± 0.17	4.86 ± 0.27	0.16 ± 0.04
C4	59968.15	0.7	0.56 ± 0.28	7.21 ± 1.59	0.85 ± 0.02
C5	59983	1.0	4.71 ± 1.28	10.0 ± 2.48	0.35 ± 0.16

Table 3. The Spearman rank correlation results obtained by correlating the γ -ray flux (upper panel) and the spectral index (α) (lower panel) with different energy band flux. Col. 1: Correlating quantities, 2: Correlation coefficient value 3: Null hypothesis probability value.

Light curves	r_s	P_{rs}
γ -ray vs X-ray	0.503	0.138
γ -ray vs V	0.84	0.002
γ -ray vs B	0.770	0.009
γ -ray vs U	0.806	0.004
γ -ray vs W1	0.770	0.009
γ -ray vs M2	0.733	0.015
γ -ray vs W2	0.770	0.009
Index(α)	r_s	P_{rs}
α vs γ -ray	-0.278	0.008
α vs X-ray	-0.115	0.751
α vs V	-0.358	0.310
α vs B	-0.358,	0.310
α vs U	-0.394	0.260
α vs W1	-0.382	0.276
α vs M2	-0.345	0.328
α vs W2	-0.382	0.276

γ -ray spectrum, are plotted with time in the lower panel of Figure 1. The MWL LC suggests a correlated trend between the γ -ray flux and index values. Consequently, we carried out a correlation analysis between the γ -ray flux and the spectral index to explore the potential existence of the "harder when brighter" feature in Ton 599. The "harder when brighter" feature is a common feature observed in most of the blazars (Britto et al. 2016; Shah et al. 2021b). The Spearman correlation coefficient and the corresponding null hypothesis probability values are obtained as $r_s \sim -0.28$ and $P_{rs} \sim 0.008$, respectively. A correlation plot between spectral indices and flux is shown in Figure 4. The index versus flux points for various components are indicated by different colours. The colour scheme differentiates between the components with higher and lower flux. Notably,

Table 4. The calculated fractional variability amplitude (F_{var}) of Ton 599 in γ -ray, X-ray and optical/UV energy bands (upper panel) during the time period MJD 59884–59992. The variability of index (α) is given in the lower panel.

Energy band	F_{var}
γ -ray (0.1–300 GeV)	0.62 ± 0.01
X-ray (0.3–10 keV)	0.17 ± 0.02
UVW2	0.32 ± 0.01
UVM2	0.32 ± 0.01
UVW1	0.31 ± 0.01
U	0.32 ± 0.01
B	0.34 ± 0.008
V	0.33 ± 0.01
Index	variability
Alpha(α)	0.09 ± 0.02

the components with brighter γ -ray flux exhibit a harder spectral index compared to those with lower flux. Overall, the results indicate a mild presence of the "harder when brighter" trend in Ton 599. Additionally, we also calculated the correlation of γ -ray index with the X-ray and Optical/UV flux values, the correlation coefficient and null-hypothesis probability values are summarized in Table 3. The obtained P_{rs} values suggest no significant correlation between γ -ray index values and X-ray/Optical-UV flux values. However, it is essential to interpret these results cautiously, given the sparse nature of the data in X-ray and optical-UV bands.

4 BROADBAND SPECTRAL ANALYSIS

In this section, we examine the fluctuations in the fundamental physical parameters responsible for the enhancement of flux during the active state (MJD 59943 – 59974) by carrying out a detailed broadband spectral study of Ton 599 using the γ -ray, X-ray, and optical/UV data. During the active state, the source has been

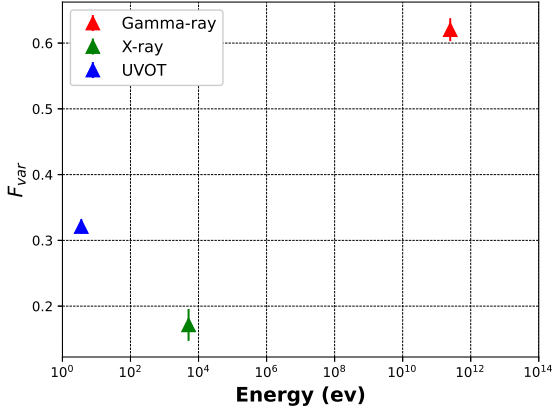


Figure 3. The fractional variability amplitude (F_{var}) of Ton 599 computed across different energy bands and plotted against energy over the time MJD 59884 – 59992.

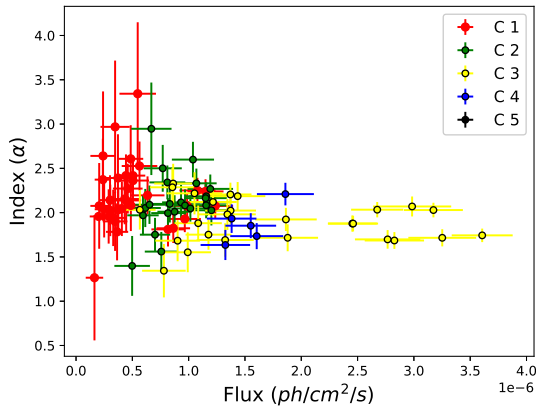


Figure 4. The Variation of spectral slope (α) with γ -ray flux for Ton 599 during the period MJD 59884 – 59992. The C 1, C 2, C 3, C 4 and C 5 are the components of the γ -ray light curve (See Figure 2)

observed 10 times by *Swift* in X-ray and optical/UV energies. We divide the MWL LC (see Figure 1) into ten flux intervals such that each state contains one *Swift* observation. The duration of each flux state is chosen to be 24 hours with centre at *Swift* observation. To obtain the γ -ray SED points for each state, we divided the total energy range 0.1 – 300 GeV into eight equally spaced bins using a logarithmic scale. For the fitting of the γ -ray spectra, we employed the log parabola model. In our analysis, the parameters of Ton 599 were allowed to vary freely, while the parameters of other sources within the Region of Interest (ROI) were kept frozen at their best-fit values obtained from fitting the γ -ray spectrum integrated over the energy range of 0.1 – 300 GeV. The X-ray spectra in different flux intervals are generated by using *xrtpipeline*, *xselect* and *ximage* tools (see Section 2.2 for details). We considered the cpflux values in order to account for the $n\text{H}$ absorption in the X-ray spectra. In *Swift*-UVOT, the images of each observation ID in different flux intervals are added together using *uvotsum* tool and optical/UV spectral points are obtained from combined images. The obtained

broadband spectral points for the selected intervals are plotted in Figure 5.

The broadband SEDs for specific flux intervals are modelled using a one-zone leptonic model. (Shah et al. 2017b; Sahayanathan et al. 2018). We consider the emission to be originating from a spherical region of radius ‘R’ within a relativistic jet characterized by a bulk Lorentz factor ‘ Γ ’. The Jet is assumed to make a small angle ‘ θ ’ to the line of sight of an observer, resulting in the Doppler boosting of the observed flux. To incorporate the Doppler boosting effect on flux, we introduce the relativistic Doppler factor (δ), defined as $\delta = [\Gamma(1 - \beta \cos \theta)]^{-1}$. We assume that the spherical emission region is filled with electrons which are distributed in energy as broken power-law (BPL), given by

$$N(\gamma)d\gamma = \begin{cases} K\gamma^{-p}d\gamma, & \gamma_{\min} < \gamma < \gamma_b \\ K\gamma_b^{q-p}\gamma^{-q}d\gamma, & \gamma_b < \gamma < \gamma_{\max} \end{cases}, \quad (6)$$

where γ is the electron Lorentz factor, K is normalization, γ_b is the spectral break energy, p and q are the particle spectral indices before and after the break. The observed flux is ascribed to synchrotron emission, a consequence of the presence of a magnetic field (B) and relativistic electrons, as well as IC emission, which includes SSC and EC processes. Isotropic blackbody external photon fields for EC process with temperatures $T \sim 1000$ K and $T \sim 42000$ K represent the IR torus and BLR photons, respectively. In FSRQs, high-energy emission involves contributions from both SSC and EC processes (Shah et al. 2017b). The spectra are calculated from synchrotron, SSC and EC emissivity functions using a numerical code which is incorporated as a local model in “*xspect*”. The resultant local model is utilized to perform the broadband spectral fitting of the source. The main model parameters include *viz.* p , q , γ_b , B , R , U_e , Θ , f , Γ and T_* , which are adjusted to achieve the best-fit SED. During the broadband SED fitting, we consider the equipartition condition between the particle energy density and magnetic energy density. Additionally, a steady-state emission is assumed in the chosen flux intervals. To account for uncertainties associated with the model, we incorporated a 12% systematic uncertainty into the data during the fitting of all the SEDs. This inclusion of a 12% systematic error enabled us to achieve a reduced χ^2 value below 2 for each of the SEDs. Due to the limited data availability at γ -ray, X-ray, and optical/UV energies, we carry out broadband SED fitting by keeping p , q , Γ , and B as free parameters, while the other parameters are fixed at typical values needed to get best-fit. The observed spectral points and the broadband SED fit along with the contributions from synchrotron, SSC and EC components are shown in Figure 5. The best-fit parameters are given in Table 5.

5 SUMMARY AND DISCUSSION

The simultaneous multi-wavelength data at optical/UV, X-ray, and γ -ray energies enabled a thorough investigation into the temporal and spectral characteristics of Ton 599 during the January 2023 flare. The γ -ray light curve exhibits a flaring activity during the period MJD 59943 – 59974, we defined this period as an active state of the source. During the January 2023 period, the daily averaged γ -ray light curve reveals the five flaring components. Figure 2 illustrates that the components C1, C2, and C3 are symmetric, while the component C4 is asymmetric. However, due to substantial error in the asymmetric parameter value of component C5, its profile is categorized as both symmetric and moderately asymmetric. The symmetric flare profile can be attributed to the time interval required

Table 5. Details of the best-fit parameters acquired in different flux intervals using one zone model. Free parameters: Col. 1. Flux states; 2, low energy particle index 3. high energy particle index, 4. Bulk Lorentz factor, 5. Magnetic field (Gauss). Fixed parameters: Col. 6. Lorentz factor corresponding to break energy; 7. Minimum Lorentz factor of electrons; 8. Integrated γ -ray flux (in units 10^{-6} ph cm $^{-2}$ s $^{-1}$), 9. χ^2 /degrees of freedom. Subscripts and superscripts on the values denote the lower and upper errors respectively, while "--" indicates that the error bound is not constrained. In all the SEDs, $\gamma_{max} = 10^6$, $R = 10^{16}$ cm, $T = 1000$ K.

State	p	q	Γ_b	B	γ_b	γ_{min}	$F_{0.1-300GeV}$	χ^2/dof
1	2.20 $^{+0.15}_{-0.20}$	4.42 $^{+0.27}_{-0.20}$	17.25 $^{+8.86}_{-4.97}$	1.52 $^{--}_{-0.14}$	2700	150	1.05	3.80/14
2	2.34 $^{+0.11}_{-0.12}$	4.92 $^{+1.09}_{-0.41}$	38.94 $^{--}_{-21.29}$	1.54 $^{--}_{-0.09}$	2400	140	0.99	14.92/16
3	2.01 $^{+0.14}_{-0.21}$	4.80 $^{+0.73}_{-0.48}$	18.08 $^{+4.07}_{-2.91}$	1.61 $^{--}_{-0.12}$	2000	150	1.37	3.78/12
4	2.10 $^{+0.15}_{-0.72}$	4.04 $^{+0.11}_{-0.11}$	28.95 $^{+10.56}_{-8.20}$	1.61 $^{+0.11}_{-0.09}$	1300	300	2.46	10.63/14
5	1.90 $^{+0.09}_{-0.09}$	4.74 $^{+0.24}_{-0.20}$	28.09 $^{+6.34}_{-4.67}$	1.66 $^{+0.05}_{-0.03}$	1950	160	2.82	21.85/15
6	1.93 $^{+0.07}_{-0.09}$	4.69 $^{+0.16}_{-0.20}$	28.8 $^{+6.78}_{-5.49}$	1.64 $^{+0.05}_{-0.02}$	1900	180	2.98	10.91/15
7	1.80 $^{+0.07}_{-0.12}$	4.61 $^{+0.17}_{-0.15}$	29.02 $^{+12.40}_{-9.82}$	1.61 $^{+0.10}_{-0.02}$	1800	180	1.87	10.23/15
8	2.03 $^{+0.15}_{-0.16}$	4.41 $^{+0.47}_{-0.27}$	46.76 $^{--}_{-11.34}$	1.63 $^{+0.13}_{-0.10}$	2100	100	1.43	4.93/14
9	1.90 $^{+0.13}_{-0.12}$	4.78 $^{+0.49}_{-0.26}$	45.76 $^{--}_{-10.49}$	1.58 $^{+0.10}_{-0.11}$	2700	90	1.21	4.33/ 14
10	2.05 $^{+0.06}_{-0.11}$	4.80 $^{+0.19}_{-0.22}$	28.65 $^{+13.56}_{-9.18}$	1.57 $^{+0.10}_{-0.02}$	2100	160	1.55	6.39/16

for particles or radiation to traverse the emission region, which is determined by spatial and geometric scales (Takahashi et al. 2000; Tanihata et al. 2001). Moreover, the overlay of short-time events can give rise to a symmetric flare (Valtaoja et al. 1999). The asymmetry in the flare profile can be attributed to rapid electron injection in an emission region followed by delayed escape or slow radiative cooling. Moreover, it can be also produced by injection of short-living energetic electrons and wider jet opening angles (Abdo et al. 2010c).

The temporal analysis of MWL LC of Ton 599 shows simultaneous and correlated variability in all the energy bands, suggesting that the broadband emission is from the same emission region and electron distribution. The increased variability amplitude in γ -rays, as compared to X-rays and optical/UV, is in accordance with results from previous blazar investigations. (e.g. Zhang et al. 2005; Shah et al. 2019; Malik et al. 2022b). Importantly, there is a similarity between the variability pattern observed in different energy bands and the shape of the SED. The broadband SED analysis reveals that the X-ray emission occurs before the break energy, indicating its origin from low-energy electrons. Contrarily, the γ -ray and Optical/UV emissions occur near or after the break energy, suggesting their association with high-energy electrons. As a result, we expect a greater degree of variability in the γ -ray energy compared to the X-ray energies. This is due to the faster cooling of high-energy electrons relative to their low-energy counterparts. The increase of flux variability with increasing energy reveals spectral variability in the source, as noted by Zhang et al. (2005).

To acquire insights into the fluctuations of physical parameters responsible for the flux enhancement during the active state (MJD 59943-59974), we divided the MWL LC into ten flux intervals and subsequently, we carried out a detailed broadband spectral study of the source in these selected intervals. During the process of broadband SED fitting, we considered the condition of equipartition between the energy density of particles and the energy density of the

magnetic field. We also assumed a steady state emission in the selected flux intervals. In our modelling approach, we employed a BPL electron distribution, which has been widely used in previous studies on blazars (e.g. Sahayanathan et al. 2018; Shah et al. 2019). A BPL electron distribution, experiencing synchrotron, SSC, and EC losses, effectively replicates the broadband emission across all flux intervals. The synchrotron process is responsible for the low-energy emission in the optical/UV energy band, while the high-energy emissions in the X-ray and γ -ray band are associated with the SSC and EC processes. We found that in all of the flux intervals, the EC scattering of IR target photons provided a satisfactory fit to the data. The resulting best-fit parameters *viz.* p , q , B and Γ for different flux intervals are shown in Table 5. The B varies in the the range of 1.52 – 1.66, which is larger than the average value of B for FS-RQs (Ghisellini & Tavecchio 2015) but falls within the physically acceptable range (Liodakis & Pavlidou 2015). Furthermore, it increases with the increase in the flux (see Table 5). The obtained spectral indices p and q vary between 1.80 – 2.34 and 4.04 – 4.92 respectively. The indices get harder as the source becomes brighter. These values of indices show that the steepness of the spectra after the break energy is greater than what would be expected from synchrotron cooling alone. This suggests that the break in the particle distribution is not solely due to cooling effects and indicates the need for an alternative explanation. One possibility is the presence of an energy-dependent diffusion coefficient. Previous studies, such as Zirakashvili & Aharonian (2007), have demonstrated that with an energy-dependent diffusion coefficient, the spectral cutoff exhibits a sub-exponential or steeper form at high energies. Moreover, in the diffuse shock particle acceleration process, the hardness or steepness of indices is determined by the shock speed, shock field obliquity, nature of particle scattering, and magnitude of turbulence (Summerlin & Baring 2012). The value of Γ ranges from 28.25 to 37.15 in all the flux intervals, and there is no apparent trend observed

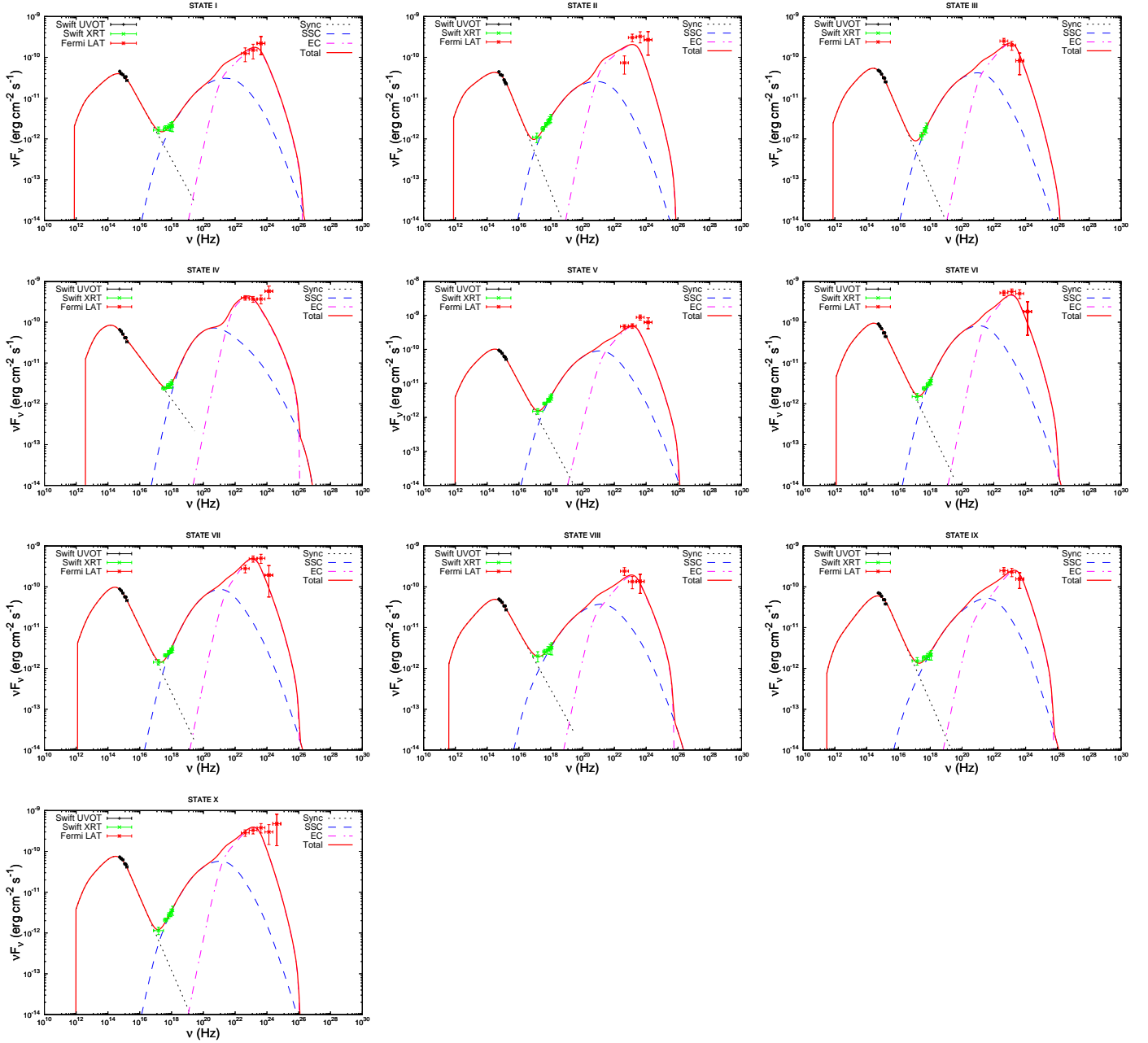


Figure 5. Broadband SEDs of Ton 599 for the ten selected flux intervals (see Table 1). The solid red colour curves represent the total (Synchrotron, SSC, EC) SED fit.

in Γ between the low and high flux emissions. The source has also been studied earlier by various authors in different flux intervals. Notably, [Rajput & Pandey \(2021\)](#) examined its 2021 flare, while [Prince \(2019\)](#) and [Patel & Chitnis \(2020\)](#) studied a high-activity state in 2017. Our best-fit parameters (B , p and q) are in agreement with those of [Patel & Chitnis \(2020\)](#), who however have fixed the value of Γ at 15. The [Rajput & Pandey \(2021\)](#) and [Prince \(2019\)](#) have focused mostly on the *Fermi* spectrum of the source and haven't carried out the broadband spectral modelling of the source. Using the broadband observations *viz.* optical/UV, X-ray and γ -ray of Ton 599, we have investigated the changes in underlying physical param-

eters during a January 2023 active state of the source. By incorporating additional data at the VHE range and conducting the broadband analysis during various active states of the source, a better constraint on the underlying physical parameters responsible for the flux variation in the source can be achieved in future research work.

6 ACKNOWLEDGEMENTS

AM, SS and NI are thankful to the Department of Atomic Energy (DAE), Board of Research in Nuclear Sciences (BRNS), Govt

of India via Sanction Ref No.: 58/14/21/2019-BRNS for the financial support. ZS is supported by the Department of Science and Technology, Govt. of India, under the INSPIRE Faculty grant (DST/INSPIRE/04/2020/002319).

7 DATA AVAILABILITY

The multi-wavelength data used in this work is publicly available at the data browse section of the respective observatories. Codes used in this work will be shared on request to the corresponding authors (email: aqibmanzoor1111@gmail.com and shahzahir4@gmail.com)

REFERENCES

- Abdo A. A., et al., 2010a, *Nature*, **463**, 919
- Abdo A. A., et al., 2010b, *ApJ*, **716**, 30
- Abdo A. A., et al., 2010c, *ApJ*, **722**, 520
- Aharonian F., et al., 2007, *ApJ*, **664**, L71
- Albert J., et al., 2007, *ApJ*, **669**, 862
- Arnaud K. A., 1996, in Jacoby G. H., Barnes J., eds, *Astronomical Society of the Pacific Conference Series Vol. 101, Astronomical Data Analysis Software and Systems V*. p. 17
- Atwood W. B., et al., 2009, *ApJ*, **697**, 1071
- Baloković M., et al., 2016, *ApJ*, **819**, 156
- Blażejowski M., Sikora M., Moderski R., Madejski G. M., 2000, *ApJ*, **545**, 107
- Boettcher M., Mause H., Schlickeiser R., 1997, *A&A*, **324**, 395
- Böttcher M., Reimer A., Sweeney K., Prakash A., 2013, *ApJ*, **768**, 54
- Britto R. J., Bottacini E., Lott B., Razzaque S., Buson S., 2016, *ApJ*, **830**, 162
- Burrows D. N., et al., 2005, *Space Sci. Rev.*, **120**, 165
- Celotti A., Ghisellini G., 2008, *MNRAS*, **385**, 283
- Chidiac C., et al., 2016, *A&A*, **590**, A61
- Costamante L., Ghisellini G., 2002, *A&A*, **384**, 56
- Dermer C. D., Schlickeiser R., 1993, *ApJ*, **416**, 458
- Dermer C. D., Schlickeiser R., Mastichiadis A., 1992, *A&A*, **256**, L27
- Fossati G., Maraschi L., Celotti A., Comastri A., Ghisellini G., 1998, *MNRAS*, **299**, 433
- Ghisellini G., Madau P., 1996, *MNRAS*, **280**, 67
- Ghisellini G., Tavecchio F., 2008, *MNRAS*, **387**, 1669
- Ghisellini G., Tavecchio F., 2015, *MNRAS*, **448**, 1060
- Ghisellini G., Maraschi L., Treves A., 1985, *A&A*, **146**, 204
- Ghisellini G., Tavecchio F., Maraschi L., Celotti A., Sbarro T., 2014, *Nature*, **515**, 376
- Glassgold A. E., et al., 1983, *ApJ*, **274**, 101
- Hewett P. C., Wild V., 2010, *MNRAS*, **405**, 2302
- Jones T. W., O'Dell S. L., Stein W. A., 1974, *ApJ*, **188**, 353
- Kalberla P. M. W., Burton W. B., Hartmann D., Arnal E. M., Bajaja E., Morras R., Pöppel W. G. L., 2005, *A&A*, **440**, 775
- Kaur N., Baliyan K. S., 2018, *A&A*, **617**, A59
- Lioudakis I., Pavlidou V., 2015, *MNRAS*, **454**, 1767
- Malik Z., Shah Z., Sahayanathan S., Iqbal N., Manzoor A., 2022b, *MNRAS*, **514**, 4259
- Malik Z., Shah Z., Sahayanathan S., Iqbal N., Manzoor A., 2022a, *Monthly Notices of the Royal Astronomical Society*, **514**, 4259
- Mannheim K., 1993, *A&A*, **269**, 67
- Mannheim K., Biermann P. L., 1992, *A&A*, **253**, L21
- Mao P., Urry C. M., Massaro F., Paggi A., Cauteruccio J., Künzel S. R., 2016, *ApJS*, **224**, 26
- Mattox J. R., et al., 1996, *ApJ*, **461**, 396
- McHardy I. M., Marscher A. P., Gear W. K., Muxlow T., Lehto H. J., Abraham R. G., 1993, *MNRAS*, **261**, 464
- Mirzoyan R., 2017, *The Astronomer's Telegram*, **10817**, 1
- Mücke A., Protheroe R. J., 2001, *Astroparticle Physics*, **15**, 121
- Mücke A., Protheroe R. J., Engel R., Rachen J. P., Stanev T., 2003, *Astroparticle Physics*, **18**, 593
- Mukherjee R., VERITAS Collaboration 2017, *The Astronomer's Telegram*, **11075**, 1
- Paliya V. S., Marcotulli L., Ajello M., Joshi M., Sahayanathan S., Rao A. R., Hartmann D., 2017, *ApJ*, **851**, 33
- Patel S. R., Chitnis V. R., 2020, *MNRAS*, **492**, 72
- Petropoulou M., Dermer C. D., 2016, *ApJ*, **825**, L11
- Poutanen J., Zdziarski A. A., Ibragimov A., 2008, *MNRAS*, **389**, 1427
- Prince R., 2019, *The Astrophysical Journal*, **871**, 101
- Raiteri C. M., et al., 2013, *MNRAS*, **436**, 1530
- Rajput B., Pandey A., 2021, γ -ray Flux and Spectral Variability of Blazar Ton 599 during Its 2021 Flare ([arXiv:2112.06681](https://arxiv.org/abs/2112.06681))
- Ramakrishnan V., et al., 2014, *MNRAS*, **445**, 1636
- Roming P. W. A., et al., 2005, *Space Sci. Rev.*, **120**, 95
- Sahayanathan S., Sinha A., Misra R., 2018, *Research in Astronomy and Astrophysics*, **18**, 035
- Schlafly E. F., Finkbeiner D. P., 2011, *ApJ*, **737**, 103
- Shah Z., Sahayanathan S., Mankuzhiyil N., Kushwaha P., Misra R., Iqbal N., 2017a, *Monthly Notices of the Royal Astronomical Society*, **470**, 3283
- Shah Z., Sahayanathan S., Mankuzhiyil N., Kushwaha P., Misra R., Iqbal N., 2017b, *MNRAS*, **470**, 3283
- Shah Z., Jithesh V., Sahayanathan S., Misra R., Iqbal N., 2019, *MNRAS*, **484**, 3168
- Shah Z., Jithesh V., Sahayanathan S., Iqbal N., 2021a, *MNRAS*, **504**, 416
- Shah Z., Jithesh V., Sahayanathan S., Iqbal N., 2021b, *Monthly Notices of the Royal Astronomical Society*, **504**, 416
- Sikora M., Begelman M. C., Rees M. J., 1994, *ApJ*, **421**, 153
- Summerlin E. J., Baring M. G., 2012, *ApJ*, **745**, 63
- Takahashi T., et al., 2000, *ApJ*, **542**, L105
- Tanihata C., Urry C. M., Takahashi T., Kataoka J., Wagner S. J., Madejski G. M., Tashiro M., Kouda M., 2001, *ApJ*, **563**, 569
- Thompson D. J., et al., 1995, *ApJS*, **101**, 259
- Ulrich M.-H., Maraschi L., Urry C. M., 1997, *ARA&A*, **35**, 445
- Urry C. M., Padovani P., 1995, *PASP*, **107**, 803
- Valtaoja E., Lähteenmäki A., Teräsanta H., Lainela M., 1999, *ApJS*, **120**, 95
- Vaughan S., Edelson R., Warwick R. S., Uttley P., 2003, *MNRAS*, **345**, 1271
- Wood M., Caputo R., Charles E., Di Mauro M., Magill J., Perkins J. S., Fermi-LAT Collaboration 2017, in *35th International Cosmic Ray Conference (ICRC2017)*. p. 824 ([arXiv:1707.09551](https://arxiv.org/abs/1707.09551)), doi:10.22323/1.301.0824
- Zhang Y. H., Treves A., Celotti A., Qin Y. P., Bai J. M., 2005, *ApJ*, **629**, 686
- Zirakashvili V. N., Aharonian F., 2007, *A&A*, **465**, 695

